Carbon Dioxide Capture for Storage in Deep Geologic Formations – Results from the CO_2 Capture Project

Geologic Storage of Carbon Dioxide with Monitoring and Verification

Volume 2

Elsevier Internet Homepage – http://www.elsevier.com
Consult the Elsevier homepage for full catalogue information on all books, major reference works, journals, electronic products and services.

Elsevier Titles of Related Interest

AN END TO GLOBAL WARMING
L.O. Williams
ISBN: 0-08-044045-2, 2002

FUNDAMENTALS AND TECHNOLOGY OF COMBUSTION
F. El-Mahallawy, S. El-Din Habik
ISBN: 0-08-044106-8, 2002

GREENHOUSE GAS CONTROL TECHNOLOGIES: 6TH INTERNATIONAL CONFERENCE
John Gale, Yoichi Kaya
ISBN: 0-08-044276-5, 2003

MITIGATING CLIMATE CHANGE: FLEXIBILITY MECHANISMS
T. Jackson
ISBN: 0-08-044092-4, 2001

Related Journals:
Elsevier publishes a wide-ranging portfolio of high quality research journals, encompassing the energy policy, environmental, and renewable energy fields. A sample journal issue is available online by visiting the Elsevier web site (details at the top of this page). Leading titles include:

Energy Policy
Renewable Energy
Energy Conversion and Management
Biomass & Bioenergy
Environmental Science & Policy
Global and Planetary Change
Atmospheric Environment
Chemosphere – Global Change Science
Fuel, Combustion & Flame
Fuel Processing Technology

All journals are available online via ScienceDirect: www.sciencedirect.com

To Contact the Publisher
Elsevier welcomes enquiries concerning publishing proposals: books, journal special issues, conference proceedings, etc. All formats and media can be considered. Should you have a publishing proposal you wish to discuss, please contact, without obligation, the publisher responsible for Elsevier's Energy program:

Henri van Dorssen
Publisher
Elsevier Ltd
The Boulevard, Langford Lane
Kidlington, Oxford
OX5 1GB, UK

Phone: +44 1865 84 3682
Fax: +44 1865 84 3931
E.mail: h.dorssen@elsevier.com

General enquiries, including placing orders, should be directed to Elsevier's Regional Sales Offices – please access the Elsevier homepage for full contact details (homepage details at the top of this page).

Carbon Dioxide Capture for Storage in Deep Geologic Formations – Results from the CO_2 Capture Project

Geologic Storage of Carbon Dioxide with Monitoring and Verification

Edited by

Sally M. Benson
Lawrence Berkeley Laboratory
Berkeley, CA,USA

and Associate Editors

Curt Oldenburg[1], Mike Hoversten[1] and Scott Imbus[2]
[1]Lawrence Berkeley National Laboratory
Berkeley, CA, USA
[2]Chevron Texaco Energy Technology Company
Bellaive, TX, USA

Volume 2

ELSEVIER
2005

Amsterdam – Boston – Heidelberg – London – New York – Oxford
Paris – San Diego – San Francisco – Singapore – Sydney – Tokyo

ELSEVIER B.V.
Radarweg 29
P.O. Box 211, 1000 AE Amsterdam
The Netherlands

ELSEVIER Inc.
525 B Street, Suite 1900
San Diego, CA 92101-4495
USA

ELSEVIER Ltd
The Boulevard, Langford Lane
Kidlington, Oxford OX5 1GB
UK

ELSEVIER Ltd
84 Theobalds Road
London WC1X 8RR
UK

First edition 2005

Library of Congress Cataloging in Publication Data
A catalog record is available from the Library of Congress.

British Library Cataloguing in Publication Data
A catalogue record is available from the British Library.

ISBN: 0-08-044570-5 (2 volume set)

Volume 1: Chapters 8, 9, 13, 14, 16, 17, 18, 24 and 32 were written with support of the U.S. Department of Energy under Contract No. DE-FC26-01NT41145. The Government reserves for itself and others acting on its behalf a royalty-free, non-exclusive, irrevocable, worldwide license for Governmental purposes to publish, distribute, translate, duplicate, exhibit and perform these copyrighted papers. EU co-funded work appears in chapters 19, 20, 21, 22, 23, 33, 34, 35, 36 and 37. Norwegian Research Council (Klimatek) co-funded work appears in chapters 1, 5, 7, 10, 12, 15 and 32.

Volume 2: The Storage Preface, Storage Integrity Preface, Monitoring and Verification Preface, Risk Assessment Preface and Chapters 1, 4, 6, 8, 13, 17, 18, 19, 20, 21, 22, 23, 24, 25, 26, 27, 28, 29, 30, 31, 32, 33 were written with support of the U.S. Department of Energy under Contract No. DE-FC26-01NT41145. The Government reserves for itself and others acting on its behalf a royalty-free, non-exclusive, irrevocable, worldwide license for Governmental purposes to publish, distribute, translate, duplicate, exhibit and perform these copyrighted papers. Norwegian Research Council (Klimatek) co-funded work appears in chapters 9, 15 and 16.

♾ The paper used in this publication meets the requirements of ANSI/NISO Z39.48-1992 (Permanence of Paper).
Printed in The Netherlands.

Carbon Dioxide Capture for Storage in Deep Geologic Formations, Volume 2
D.C. Thomas and S.M. Benson (Eds.)

Chapter 7

GEOPHYSICAL AND GEOCHEMICAL EFFECTS OF SUPERCRITICAL CO_2 ON SANDSTONES

Hartmut Schütt, Marcus Wigand and Erik Spangenberg

Geo-Research-Center (GFZ) Potsdam, Potsdam, Germany

ABSTRACT

The overall objective of this laboratory study was to investigate the geophysical and geochemical effects of CO_2 storage in deep saline formations. We used a triaxial cell and autoclaves to reproduce reservoir pressure and temperature conditions that are representative of depths down to 2000 m. The CO_2 is in the supercritical state ($CO_{2,scr}$) at depths greater than approximately 800 m. We measured a number of geophysical parameters, such as seismic wave speeds and attenuation, and collected liquid samples that had been in contact with the rock. Geochemical reactions were studied in detail in autoclaves that are charged with either milled rock or mineral separates. We used three sandstone samples as reservoir rock, and 1 M NaCl solution in doubly deionized water as brine. The geophysical data showed that some effects were qualitatively predictable by standard models. The Gassmann model predicted the dependence of the saturating fluid on the bulk modulus, but underestimated the measured results by approximately 10%. This discrepancy may be due to the modulus dispersion between the low-frequency range of the Gassmann model and the ultrasonic laboratory frequency. The Voigt model reproduced the saturation dependence of v_p. Some experiments, however, indicated the existence of fluid front instabilities by reaching only 50% saturation. This corroborated the results of numerical modeling qualitatively. Unexpected was the increase of the compressional wave attenuation for $CO_{2,scr}$ saturation. Scattering can be excluded as a cause, and a local fluid flow model failed to predict the observed effect. Also unexpected and not predicted by the Gassmann equations was the dependence on the saturating fluid of the shear modulus, which is a few percent smaller for $CO_{2,scr}$ saturation than for brine saturation. This may be caused by fluid–mineral interactions. Mineralogical analysis of the rock before and after CO_2 flooding indicated that the concentration of major and trace elements decreased, whereas the Si content increased. The mobilization and removal of these elements was caused by the alteration of rock-forming minerals, e.g. biotite, plagioclase, alkali feldspar. Furthermore, we observed the mobilization of heavy metal cations. Precipitation of mineral phases (e.g. dawsonite) was not observed in the short-term experiments. We are still lacking a thorough understanding of the correlation between geophysical and geochemical data. Long-term experiments (duration of several weeks) and careful analysis on a smaller length-scale (individual grains and grain contacts) may help to address this issue.

INTRODUCTION

Geological storage of CO_2 has the potential to reduce the net CO_2 emissions of industrialized countries significantly, while still allowing for the use of fossil fuels. The storage of large amounts of CO_2 requires careful planning of the technical operations and prediction of the long-term behavior of the entire system (fluids, reservoir rock, cap rock, overburden) to minimize risks and to address public concerns about safety. Some key questions are given below.

- What is the long-term fate of the CO_2? How much will dissolve in brine, and how much will be trapped in newly precipitated minerals?
- Will the CO_2 dissolve and/or precipitate minerals in the reservoir, thereby changing the transport properties of the reservoir rock (sealing the reservoir or opening pathways)?
- Will the CO_2 affect the pressure in the reservoir and/or the stability of the reservoir (risk of subsidence)?

- Can geophysical methods (active and passive, surface and borehole) provide reliable data to assess the saturation and pressure state of the reservoir?
- Is there a correlation between geophysical data and geochemical processes in the reservoir?

Answering these questions requires—besides numerical modeling—careful experiments in the laboratory on reservoir and cap rock samples under realistic and controlled conditions. These measurements are needed to verify numerical results and calibrate geophysical and geochemical field measurements. The results may help to develop more realistic long-term storage and risk assessment scenarios.

CHEMICAL AND PHYSICAL PROPERTIES OF BRINE AND SUPERCRITICAL CO_2

The sodium chloride content of the brine was adjusted to saline formation compositions occurring in the North German basin [1,2] using sodium chloride (analytical grade) and deionized water. The composition of the initial 1 M brine (58.44 g/L NaCl) (L0), analyzed by inductively coupled plasma optical emission spectroscopy (ICP-OES) and ICP mass spectrometry (ICP-MS), is summarized in Table 6.

The critical temperature is the highest temperature at which a gas can be converted to a liquid by an increase in pressure; the critical pressure is the highest pressure at which a liquid can be converted to a gas by an increase in temperature [3], cf. Figure 1. A supercritical fluid possesses properties that are both gas and liquid-like. Figure 2a–c shows some isothermal ($T = 60$ °C) physical properties of CO_2 and brine that are relevant for seismic wave propagation in saturated porous rocks. The pressure and temperature conditions are representative of the experiments. The properties of the brine are virtually independent of pressure, while the properties of CO_2 change substantially. The density of CO_2 (300–600 kg/m^3) is of the order of the brine density (1000 kg/m^3), while the CO_2 viscosity and bulk modulus are 1–2.5 orders of magnitude smaller than the respective properties of brine (Figure 3). These pronounced viscosity and bulk modulus contrasts between brine and CO_2 can be expected to cause substantial changes in seismic attributes, such as seismic wave speeds and attenuation. This may allow for the detection of saturation as well as pore pressure changes and for monitoring the reservoir conditions during CO_2 storage using seismic surface and borehole methods.

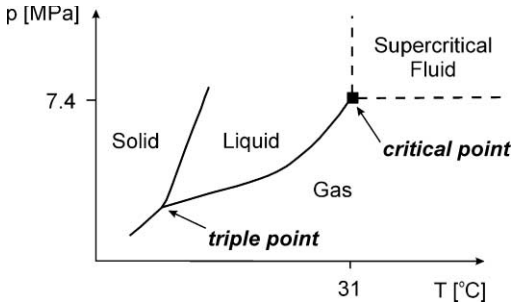

Figure 1: Phase diagram for CO_2 (modified from http://www.dekker.com/servlet/product/DOI/101081EECHR120005324).

SAMPLE DESCRIPTION

Three different types of sandstone were selected to represent reservoir rocks. They differ mainly by their porosity, permeability and grain size (Table 1). These sandstones are litharenites and sub-litharenites (Figure 4). They contain mainly quartz with variable amounts of feldspar (alkali feldspar, plagioclase) and clay minerals (mainly sericite, illite, kaolinite and glauconite). Chemical alteration of feldspars is common and typically involves replacement by clay minerals (e.g. sericite, kaolinite and illite) [4]. The common accessory minerals are zircon, apatite, tourmaline and rutile. Individual chlorite and muscovite crystals are also present in the sandstone samples BW3 and BW6. In contrast to sample H2, the samples BW3 and BW6

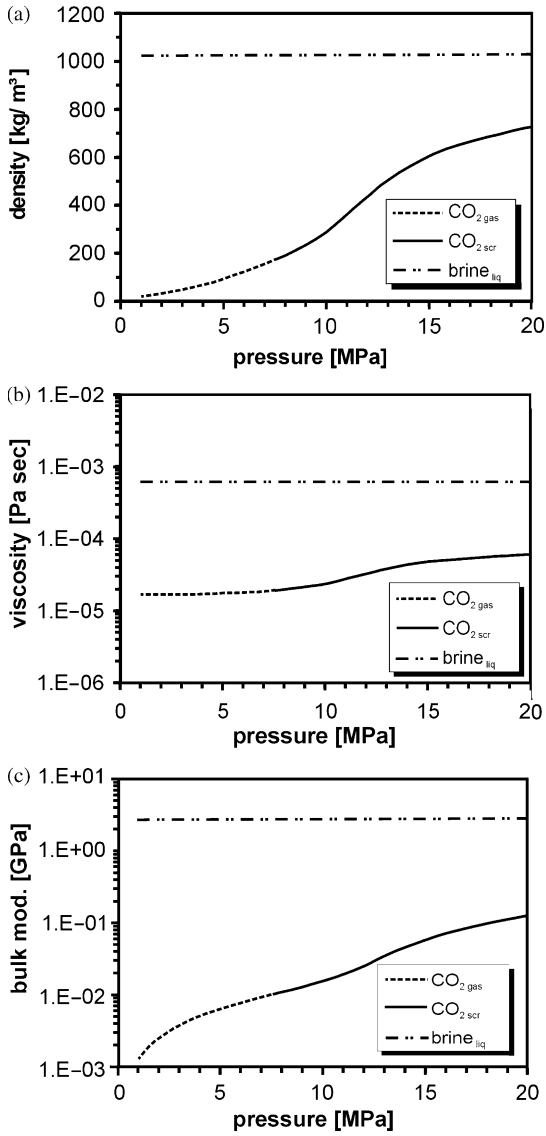

Figure 2: Physical properties of 1 M brine and CO_2 as function of pressure at 60 °C. The properties of brine are virtually constant over the entire pressure range, while the CO_2 properties change substantially. Data are from the NIST database, http://webbook.nist.gov/chemistry/.

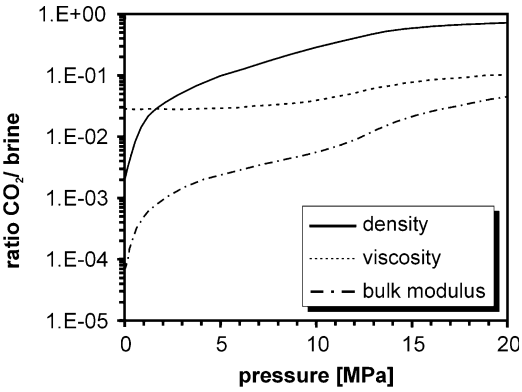

Figure 3: Ratio of the CO_2 and brine properties from Figure 2. The CO_2 density is similar to that of brine in this pressure range, while the viscosity and the bulk modulus are substantially smaller for CO_2 than for brine. Data are from the NIST database, http://webbook.nist.gov/chemistry/.

contain calcite as secondary mineral phases in minor amounts. The matrix of all samples contains abundant opaque iron oxide. Lithic fragments are present in all samples. The lithic fragments in BW3 and BW6 are commonly chert and clay schist. The cement of the sandstone samples consists of silica and clay, whereas the cement fraction varies from 3 to 11%. The quartz cement in all examined samples is in the form of overgrowths of detrital grains. Some of the quartz grains are coated with a thin rim of hematite and limonite cement. The amount of clay cement increases from H2 over BW3 to BW6.

TABLE 1
SAMPLE DESCRIPTION OF RESERVOIR ROCK SAMPLES

Sample	**H2**	**BW3**	**BW6**
Locality[a]	Diemelstadt	Heilbronn	Wertheim-Dietenhahn
Character[a]	Wrexener sandstone	Heilbronner sandstone	–
Classification	Sub-litharenite	Litharenite	Sub-litharenite
Formation[a]	Mittl. Bunt-Sst.	Schilf-Sst. (km2)	(sm1) sandstone
Grain size[a]	Medium-grained, 200–630 μm	Fine-grained, 70–180 μm	Fine-medium grained, 125–630 μm
Sorting[a]	Poorly	Moderately to well	Well
Cement[a]	Mainly silica, clay, growth of microgranular quartz and kaolinite, illite/sericite	Clay, additional silica and limonite	Clay, additional silica, hematite and limonite
Cement fraction (%)[a]	3	11	4
Porosity ϕ (%)[b]	20	22.24	16
Permeability K_{air} (mD)[b]	203.7–379.4	0.767	0.24–0.81

Sst.: sandstone.
[a] Ref. [5].
[b] U. Trautwein, personal communication, 2003. Classification after Ref. [6].

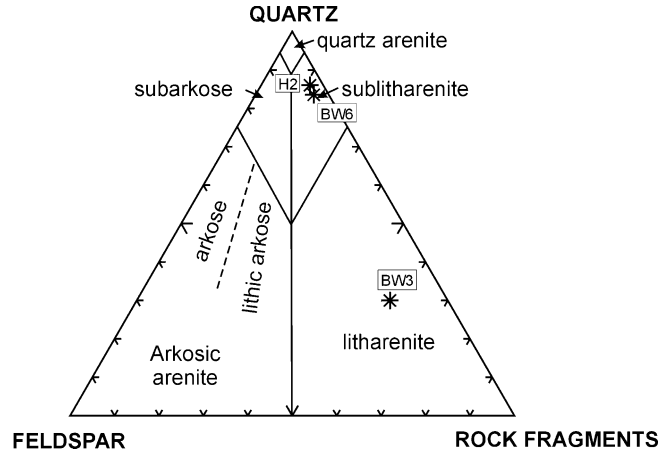

Figure 4: Classification of sandstone samples. The diagram is modified after Ref. [4]. The matrix fraction (i.e. grains <30 μm) is $<15\%$ in all sandstone samples.

EXPERIMENTS IN THE TRIAXIAL CELL

A description of the triaxial apparatus (Figure 5) can be found in Ref. [7]. The triaxial cell can be heated externally. The fluids are pushed through the sample in the triaxial cell with two pairs of pumps. Each pair consists of an upstream and a downstream pump, which create a pressure difference between the opposite ends of the sample. While one upstream and one downstream pumps are connected to the sample, the other two pumps get fluid from a reservoir or dispose off fluid into a container. This ensures a continuous flow through the sample. The fluid reservoirs can be exchanged while the sample is in the triaxial cell. This allows for alternating brine and CO_2 floods (so-called water-alternating-gas (WAG) tests). During the experiment, liquid (brine) samples can be taken from the collecting reservoir. The liquid is analyzed for ions that were mobilized by chemical reactions between brine, CO_2 and the minerals.

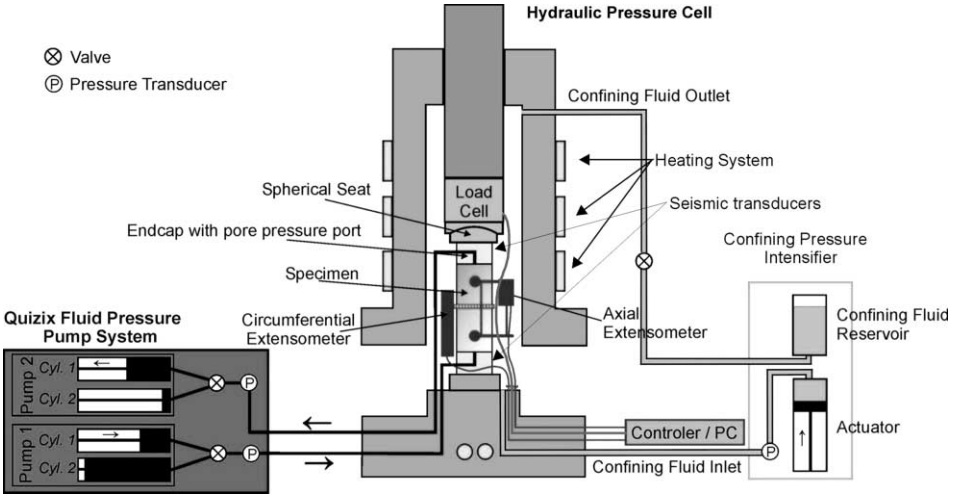

Figure 5: Sketch of the triaxial cell with the pump and heating systems.

The seismic compressional and shear wave speeds (v_p, v_s) are measured by passing an ultrasonic wave through the sample ($f \approx 0.5$ MHz). The waveforms are stored, and v_p and v_s are calculated from the travel times. The seismic wave attenuation is assessed using the spectral ratio method [8]. The waveforms of the dry samples are used as a low-attenuation reference. Lateral and axial strain data as well as temperature, stress and fluid pressure are measured at pre-selected time intervals.

The dry sandstone samples are of cylindrical shape, have a diameter of 50 mm and are 100 mm long. The shape of the samples is limited by the dimension and assembly of the triaxial cell. They are heated to 40 or 60 °C (Table 2) and the confining pressure is increased at a rate of 0.5 MPa/min to 30 MPa. The sample is allowed to settle at the new conditions for 1 day before v_p and v_s are measured. The sample is then saturated with brine and the pore pressure is raised in steps at a rate of 0.5 MPa/min. v_p and v_s are measured at several intermediate pore pressure levels after the sample has been allowed to settle for about 30 min. Brine is then passed through the sample at flow rates of 1–10 mL/min. The seismic wave speeds are measured at different pore pressure levels. In the next saturation step the brine is displaced by $CO_{2,scr}$. The measurements are equivalent to those conducted during brine saturation. After the last brine flood, the system is rinsed with deionized water to flush the salt out of the entire system. The duration of the saturation with each fluid corresponds to the porosity and permeability of each sample and is given in Table 2. In contrast to the other samples, BW3 was saturated with $CO_{2,scr}$ twice.

The in-vessel load cell of the MTS and QUIZIX pumps, which are in contact with the fluids during the experiments, are made of different types of stainless steel. The compositions of the steel types are given in Table 3.

The corrosion rate of stainless steel increases with increasing chloride ion content over the range from 10,000 to 100,000 ppm. The magnitude of this effect increases with increasing temperature over 60 °C. Corrosion intensity generally increases with CO_2 partial pressure. CO_2 is an acid gas, i.e. it has the ability to lower the pH when it is dissolved in an aqueous solution such as the 1 M NaCl brine. This increased aggressiveness results from the decrease of the pH of the aqueous phase as the partial pressure of CO_2 increases and leads to the mobilization of cations, which are components of stainless steel.

To avoid errors in the interpretation of the fluid data, a flow-through experiment under 60 °C and 15 MPa pore pressure was conducted on a chemically inert polytetrafluoroethylene (PTFE) cylinder with a centered drill-hole of diameter of 0.2 mm to evaluate the corrosion behavior of the steel. The PTFE cylinder has the same dimension and design as the sandstone samples. The results of this experiment are given in Table 4.

The pH was measured in partially degassed brine after the sampling of the fluid at 25 °C and atmospheric pressure. The initial pH of the 1 M NaCl brine (6.9) decreased to 5.9 and 5.5 after the saturation steps containing a mixture of 1 M NaCl and $CO_{2,scr}$ (Table 4). In the first saturation step, the PTFE cylinder was flushed with 1 M NaCl brine over a time span of 24 h. Under these circumstances, the chloride content of the aqueous phase does not affect corrosion of the steel. The concentrations of all analyzed cations are below the detection limit (Table 4). The 1 M NaCl brine was displaced by $CO_{2,scr}$ after 24 h. A 49 h contact of $CO_{2,scr}$ with the steel results in an increase of the Mn, Si, Ni, Mo and Fe contents of the sampled fluid. The concentrations of these cations increase in the fluid after the displacement of the $CO_{2,scr}$ by 1 M NaCl. Elements such as Cr, Co, W and V were not mobilized after the reaction of the steel with the fluid in measurable amounts.

ANALYTICAL METHODS

Major and trace element abundances were determined by X-ray fluorescence (XRF) (Philips PX 1400 with a Rh tube) and ICP-MS (VG Plasma Quad PQ^{2+}) at the Geo-Research-Center (GFZ) Potsdam using the method described in Ref. [9]. H_2O and CO_2 contents were measured with infrared spectrometry (LECO CH analyzer) in a 1000 °C oxygen stream. Solids were analyzed using optical microscopy and X-ray diffraction (XRD). Mineral phases were determined by XRD analysis using a Cu tube at 40 kV and 20 nA (wavelength Cu Kα). Hydrothermal fluids were periodically sampled during the experiments and analyzed. A defined volume of these hydrothermal fluids was mixed with 6 N HCl (Baker ULTREX) to dissolve oxide and hydroxide precipitates. Dissolved Si, Ca, K, Fe, Mg, Mn, and Zn were determined by inductively coupled plasma atomic emission spectrometry (Varian Liberty 200) at the Geo-Research-Center Potsdam.

TABLE 2
CONDITIONS OF THE FLOW-THROUGH EXPERIMENTS

Sample	T (°C)	Confining pressure (MPa)	Pore pressure (MPa)	Total duration of saturation of each sample (h)	Duration of saturation with 1 M NaCl (h)	Duration of saturation with $CO_{2,scr}$ (h)	Duration of saturation with 1 M NaCl (h)	Duration of saturation with $CO_{2,scr}$ (h)	Duration of saturation with deionized water (h)
T	60	30	15	149	24	49	72	–	4
H2	40	25	13	92	20	31	31	–	10
BW3	60	30	15	152	22	21	27	72	10
BW6	60	30	15	83	25	24	24	–	10

–, not performed.

TABLE 3
TYPE AND COMPOSITION OF THE STEEL TYPES, WHICH ARE IN CONTACT WITH THE FLUIDS DURING THE EXPERIMENT

(%)	X35CrMo17	X5CrNiMo1712.2	Hastelloy
C	0.38	0.08 max.	0.010
Mn	1.00 max	2.00 max.	1.00
P	–	0.045 max.	0.025
S	1.00 max	0.030 max.	0.010
Si	–	0.75 max.	0.08
Cr	16.00	16.00–18.00	15.50
Ni	0.80	10.00–14.00	57.00
Mo	1.00	2.00–3.00	16.00
Fe	Balance	Balance	5.50
Co	–	–	2.50
W	–	–	4.00
V	–	–	0.35

Balance; –, not given.

TABLE 4
CHEMICAL COMPOSITION OF FLUID SAMPLES AFTER FOUR STAGES OF SATURATION OF THE PTFE CYLINDER

Sample	T (PTFE cylinder)		
pH[b]	6.9 Saturation with 1 M NaCl	5.9 Saturation with supercritical CO_2	5.5 Saturation with 1 M NaCl
mg/l			
Mn	b.d.l.[a]	0.19	0.46
P	n.a.[c]	n.a.[c]	n.a.[c]
S	n.a.[c]	n.a.[c]	n.a.[c]
Si	b.d.l.[a]	0.2	2.1
Cr	b.d.l.[a]	b.d.l.[a]	b.d.l.[a]
Ni	b.d.l.[a]	2.1	8.2
Mo	b.d.l.[a]	0.1	0.5
Fe	b.d.l.[a]	1.0	45
Co	b.d.l.[a]	b.d.l.[a]	b.d.l.[a]
W	b.d.l.[a]	b.d.l.[a]	b.d.l.[a]
V	b.d.l.[a]	b.d.l.[a]	b.d.l.[a]

The cations were analyzed by ICP-MS and ICP-OES. The concentrations (mg/L) are normalized to the concentrations of initial 1 M NaCl brine.
[a] b.d.l., below detection limit.
[b] pH reported is stable value measured on sampled brine at standard temperature (25 °C) and at least partially degassed.
[c] n.a., not analyzed.

Concentrations of Al, Li, Co, Ni, Cu, Mo, Cd, Sn, Tl, Th, U and Pb were determined by ICP-MS (VG Plasma Quad PQ^{2+}) at the GFZ following the method described in Ref. [9].

RESULTS

Seismic Wave Speeds

The simultaneous use of compressional and shear waves allows for the assessment of both the bulk and shear moduli of the saturated rock [8]. We assume that full saturation is reached after several hours of pumping fluid through the sample, but we cannot evaluate intermediate saturation states directly. To estimate saturation effects, we calculate the Voigt and Reuss bounds of the compressional wave speed [8], for the system minerals/brine/$CO_{2,scr}$. The Voigt bound represents high-frequency laboratory data, while the Reuss bound represents low-frequency field data. We assume that the shear modulus is independent of the saturation state (Gassmann model, [8]). We can then predict the Voigt and Reuss bounds of the bulk modulus and the compressional wave speed for any saturation state. The result is shown in Figure 6 for sample BW3 at 60 °C and 15 MPa pore pressure.

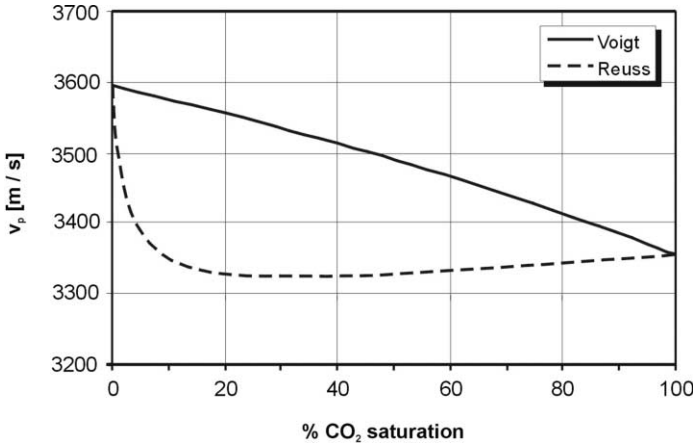

Figure 6: Predicted upper and lower bounds for the compressional wave speed as function of the CO_2 saturation for sample BW3. The Voigt bound represents the high-frequency laboratory data, the Reuss bound represents low-frequency field data. Note that both bounds are equal for full brine and full CO_2 saturation.

The wave speeds were measured at different pore pressures. They are shown in Figure 7 along with the Voigt/Reuss predictions for full brine and full $CO_{2,scr}$ saturation. At relatively low pressure, the velocity data fall along the upper bound in case of full brine saturation. For full CO_2 saturation, they fall along the lower bound. Superimposed is a pressure trend, indicated by the broken lines; the higher the pore pressure, the lower the v_p. This trend is expected, since increasing pore pressure opens small pores and cracks and reduces the moduli. The effect is more pronounced for CO_2 saturation than for brine saturation. The data at 15 MPa pore pressure in the middle between the data for full brine and full CO_2 saturation may reflect an intermediate saturation state, where both phases are present in the pores. We can now estimate the CO_2 saturation using the Voigt bound from Figure 6. It shows an almost linear decrease of v_p with increasing CO_2 saturation at a rate of 2.5 m/s per 1% CO_2. We assume that this rate is also applicable to seismic wave speeds that are measured at variable pore pressure. This approach suggests a partial CO_2 saturation of approximately 50% for the intermediate wave speeds at 15 MPa (Figure 7), since the corresponding data points fall in the middle between the upper and the lower Voigt bound under consideration of the pore pressure (broken lines in Figure 7). We can assess the approximate saturation resolution from the Voigt

bound; if the wave speeds can be resolved in 1% steps, the corresponding CO_2 saturation can be resolved in 20% steps (cf. Figure 6). The variation with CO_2 content will be more pronounced in "softer" rock samples with lower moduli and wave speeds, i.e. seismic methods will be more sensitive to saturation changes in soft rocks and unconsolidated sands. Laboratory calibration of the saturation–velocity characteristics for each reservoir rock is a prerequisite for a successful application to seismic field data, and the velocity dispersion between laboratory and field seismics has to be accounted for.

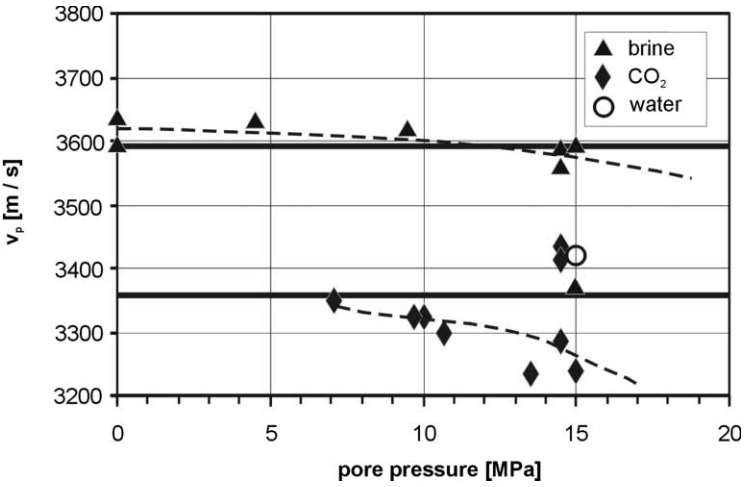

Figure 7: Compressional wave speed for sample BW3 at different saturation states and pore pressures. The heavy horizontal lines correspond to the end values (i.e. for 0 and 100% $CO_{2,scr}$ saturations, respectively) of the bounds in Figure 6. The broken lines are the trends of v_p with changing pore pressure: the higher the pore pressure, the lower the v_p.

CO_2 saturation

Ferer et al. [10] compute the CO_2 saturation at breakthrough in simple pore models for CO_2 displacing brine. They find breakthrough saturations of approximately 20% at a representative viscosity ratio M ($M = \eta_{CO_2}/\eta_{brine} = 0.05$) for a wide range of capillary numbers[1] Ca ($10^{-5} < \mathrm{Ca} \leq 10^{-2}$). For the (unrealistic) viscosity ratio of 1.0, the CO_2 saturation at breakthrough increases from 20% at $\mathrm{Ca} = 6 \times 10^{-6}$ to 50% at $\mathrm{Ca} = 6 \times 10^{-3}$. These data suggest that fluid front instabilities may occur when low-viscosity and low-density supercritical CO_2 displaces brine. This may lead to both viscous destabilized and gravity destabilized flow [11], resulting in a reduced CO_2 sweep efficiency. We estimate the capillary number for our experiment with sample BW3 from the flow rate. The data fall into the transition zone between stable displacement, viscous fingering and capillary fingering when plotted in the M–Ca plane [12]. This suggests that some sort of fluid front instability will occur under the conditions of the simulations and experiments. This may lead to a final CO_2 saturation below 1. It is not clear, however, whether this will be a significant effect under field conditions, and why there is an inconsistency between the breakthrough saturation of Ferer et al. [10] (20–50%) and our data (50–100%).

Moduli

The seismic wave speeds depend on an appropriate modulus and on the density [8]. The equations suggest that the velocities decrease/increase with increasing/decreasing density. However, opposite velocity trends

[1] The capillary number, Ca, is equal to the ratio of the viscous force to the capillary force; $\mathrm{Ca} = v\eta/\sigma$, where v is the average speed of the liquid, η the viscosity and σ the surface tension.

are frequently observed. This behavior is caused by the dependence of the moduli on the saturation state. Seismic wave speeds are usually dominated by modulus effects, while density effects are secondary.

The simultaneous use of compressional and shear waves allows for the decomposition of the measured seismic wave speeds into bulk and shear moduli [8]. The effects of saturation and pore pressure on the moduli can then be assessed. The standard model for the prediction and interpretation of fluid substitution effects are the Gassmann equations [8]

$$K_{\mathrm{sat}} = K_{\mathrm{dry}} + \frac{\left(1 - \frac{K_{\mathrm{dry}}}{K_{\mathrm{s}}}\right)^2}{\frac{\phi}{K_{\mathrm{fl}}} + \frac{1-\phi}{K_{\mathrm{s}}} - \frac{K_{\mathrm{dry}}}{K_{\mathrm{s}}^2}} = K_{\mathrm{dry}} + \Delta K \tag{1}$$

$$\mu_{\mathrm{sat}} = \mu_{\mathrm{dry}} \tag{2}$$

where K_{sat} is the bulk modulus of the liquid-saturated rock, K_{dry} the bulk modulus of the dry[2] rock, K_{s} the bulk modulus of the solid matrix material, K_{fl} the bulk modulus of the fluid, ϕ the porosity, μ_{sat} and μ_{dry} the shear moduli of the fluid-saturated and the dry rocks, respectively.

The modulus increment, ΔK, is caused by the fluid, i.e. the fluid "stiffens" the dry rock and increases v_{p}. If the fluid is a gas with low bulk modulus, this effect is negligible. The Gassmann equations hold strictly only for static deformation. They are, however, routinely applied to data from field seismics or even to ultrasonic laboratory data. This may lead to erroneous results. According to the Gassmann equations, the shear modulus is independent of the saturating fluid. This may not be true if the liquid interacts physically or chemically with the minerals, e.g. through dehydration or mineral dissolution.

The bulk moduli of sample BW3 for different saturation conditions are shown in Figure 8 as a function of the differential pressure, $p_{\mathrm{diff}} = p_{\mathrm{confining}} - p_{\mathrm{pore}}$ [13]. The confining pressure is constant (30 MPa), while the pore pressure is changed. The Gassmann prediction for brine saturation[3] is about 10% smaller than the measured value. This may be caused by the modulus dispersion, i.e. the increase of the modulus between the frequency range of the Gassmann equations (static) and the frequency range used in the laboratory (ultrasonic). The Gassmann prediction for CO_2 saturation is not shown here. It is practically identical to the dry modulus due to the high compressibility of the supercritical CO_2. It is not clear why some data at low differential pressure (i.e. high pore pressure) fall in the middle between CO_2 and brine saturation. It may be an indication of an intermediate saturation state with both brine and CO_2 present in the pores. The general picture is the same for samples H2 and BW6 in that the bulk modulus for $CO_{2,\mathrm{scr}}$ saturation is identical to the dry bulk modulus and the moduli for brine saturation are larger than the predicted moduli by approximately 9 and 12%, respectively.

The Gassmann model predicts no effect of the saturating fluid on the shear modulus, i.e. $\mu_{\mathrm{sat}} = \mu_{\mathrm{dry}}$ for all fluids. Figure 9 shows the shear moduli of sample BW3 as a function of the differential pressure for different saturation conditions. The dry modulus is the highest. Once the sample is saturated with brine, the shear modulus drops by 3% at 0 pore pressure ($p_{\mathrm{diff}} = 30$ MPa). The shear modulus depends almost linearly on the differential pressure and drops by 6% between 0 pore pressure and 15 MPa. The shear modulus drops by another 3% when brine is replaced by $CO_{2,\mathrm{scr}}$. The shear modulus also depends linearly on the differential pressure for $CO_{2,\mathrm{scr}}$ saturation. These trends are reproducible for alternating $CO_{2,\mathrm{scr}}$ and brine saturation. The shear modulus decreases for sample H2 by 5% for the first brine saturation and 4% for the $CO_{2,\mathrm{scr}}$ flood; the corresponding values for sample BW6 are 7 and 5%, respectively. The measurements show that, contrary to the Gassmann equations, the shear modulus does depend on the saturating fluid. It drops by a few percent when the dry sample is saturated with brine and by another few percent when the brine is displaced by supercritical CO_2. There seems to be a nearly linear dependence between the shear modulus and the differential pressure.

[2] Dry refers here to *drained* conditions, where the pore pressure is constant during the compression ("open" boundary condition).

[3] We assume a pure quartz matrix, $K_{\mathrm{quartz}} = 37$ GPa [8].

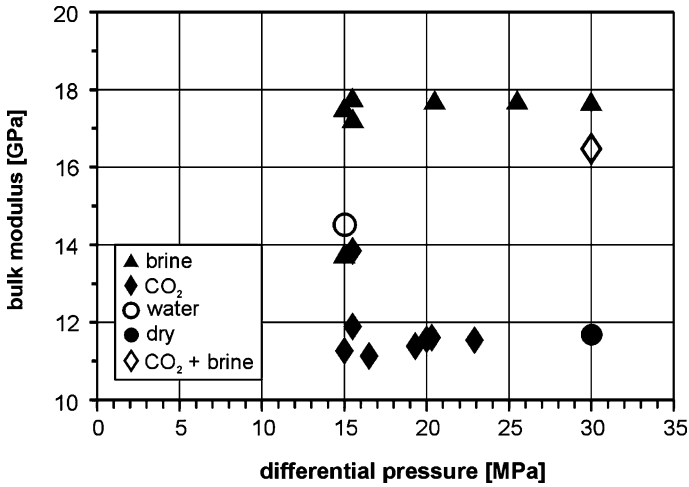

Figure 8: Measured bulk moduli for sample BW3 at different pressure and saturation conditions; the pressure is given as differential pressure $p_{\text{diff}} = p_{\text{conf}} - p_{\text{pore}}$, with $p_{\text{conf}} = 30$ MPa.

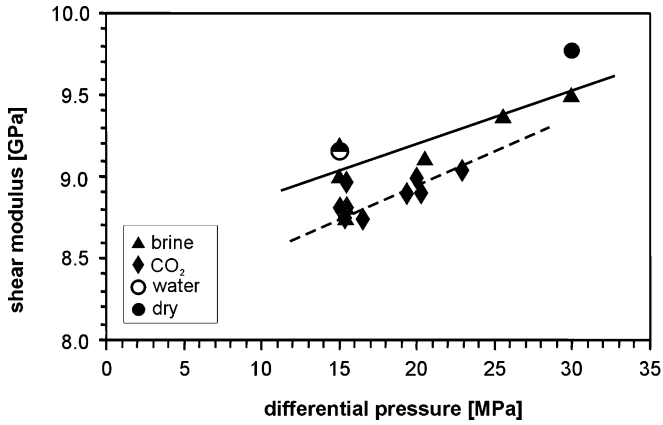

Figure 9: Measured shear moduli for sample BW3 as function of the differential pressure.

A comparison of Figures 8 and 9 shows that the bulk modulus depends mainly on the saturating fluid, while the pressure dependence is nearly negligible. On the other hand, the shear modulus depends on both the saturating fluid and the pressure. To quantify this dependence, we define the pressure sensitivity of the moduli with respect to the differential pressure, S_{pdiff}:

$$S_{\text{pdiff}} = \frac{1}{M}\frac{\mathrm{d}M}{\mathrm{d}p_{\text{diff}}} \tag{3}$$

where M is either the bulk modulus, K, or the shear modulus, μ; p_{diff} is the differential pressure, $p_{\text{diff}} = p_{\text{conf}} - p_{\text{pore}}$ [13].

The measured data suggest a linear dependence of the moduli on the differential pressure, i.e. dM/dp_{diff} is independent of p_{diff}. We can now easily evaluate the pressure sensitivities of both bulk and shear moduli for different saturation conditions using Eq. (3) and the data in Figures 8 and 9. We get approximate sensitivities of 4×10^{-3} and 3×10^{-3} MPa^{-1} for the shear modulus with brine and with $CO_{2,scr}$ saturation, respectively, while the corresponding values for the bulk modulus are 3×10^{-4} MPa^{-1} with brine and 1×10^{-3} MPa^{-1} with $CO_{2,scr}$. The shear modulus is more sensitive to the differential pressure than the bulk modulus. It is not clear why there is a difference between brine and CO_2 saturations. Neither is it clear why the bulk modulus is more sensitive for CO_2 saturation, while the shear modulus is more sensitive for brine saturation. The results demonstrate, however, that the different magnitudes of pressure and saturation sensitivities of the moduli may be used to discriminate between pressure and saturation effects using seismic v_p and v_s data. This corroborates the findings of Wang et al. [14]. However, the different frequency ranges of field and laboratory measurements have to be considered carefully before the laboratory results can be applied directly to the interpretation of field data.

Seismic Wave Attenuation

Seismic wave amplitudes decrease as the wave travels through a medium. This is due to the irreversible conversion of a fraction of the wave energy into heat.[4] Possible mechanisms of attenuation are scattering at small inhomogeneities, friction or fluid-related effects. Scattering can be excluded as a significant mechanism by applying the analysis of Aki and Richards [15]. Global fluid flow effects [16] cause significant attenuation in high-porosity and high-permeability media, such as unconsolidated sand [17], while they are often negligible in consolidated sedimentary rock [18]. Local fluid flow models [19] and squirt flow models [20] relate the attenuation to viscous dissipation in compliant pores, e.g. in penny-shaped cracks or grain contacts. This mechanism is found to cause substantial attenuation even at high hydrostatic pressure where many of the compliant pores can be expected to be closed [18].

The seismic wave attenuation can be expressed in terms of the quality factor Q, where lower Q implies larger attenuation. In terms of energies, the attenuation can be expressed as (cf. [8]):

$$\frac{1}{Q} = \frac{1}{2\pi} \frac{\Delta E}{E_{max}} \tag{4}$$

where ΔE is the energy dissipated per cycle and E_{max} the peak strain energy during the cycle.

A popular method to estimate $1/Q$ from both laboratory and field data is the spectral ratio method [8]. The logarithmic ratio of the spectral amplitudes of two signals, $\ln[A_2(f)/A_1(f)]$, is plotted as a function of the frequency, f. A_1 is a reference signal, measured in a medium with low attenuation. Aluminum serves often as the reference medium, while we use the dry sample as the reference. Dry rock usually exhibits an attenuation that is about one order of magnitude lower than saturated rock. The use of the dry sample as reference has the advantage that both signals are measured on the same piece of rock without changing the setup. This ensures identical source and receiver coupling conditions and thus very similar signal characteristics for both measurements.

Figure 10 shows the attenuation data for sample BW3. We can identify some characteristics despite the scatter in the data. The attenuation increases with increasing pore pressure (i.e. with decreasing differential pressure). This can easily be explained with opening micropores and microcracks that promote either friction along crack and grain surfaces or local fluid flow in compliant low-aspect ratio pores. Another feature is the dependence of the p-wave attenuation on the saturating fluid; it is significantly higher for $CO_{2,scr}$ saturation than for brine saturation. This dependence is not observed for the shear attenuation.

Figure 11 shows how the seismic wave attenuation may help to create a classification scheme for saturation assessment. Brine saturation is characterized by relatively high values of K/μ and Q_p/Q_s, while $CO_{2,scr}$ saturation is characterized by low values. This is true for all three sandstone samples. Note that the water-saturated sample BW3 (when deionized water is used to flush the salt out of the apparatus) lies in the domain

[4] Geometric spreading is negligible under laboratory conditions.

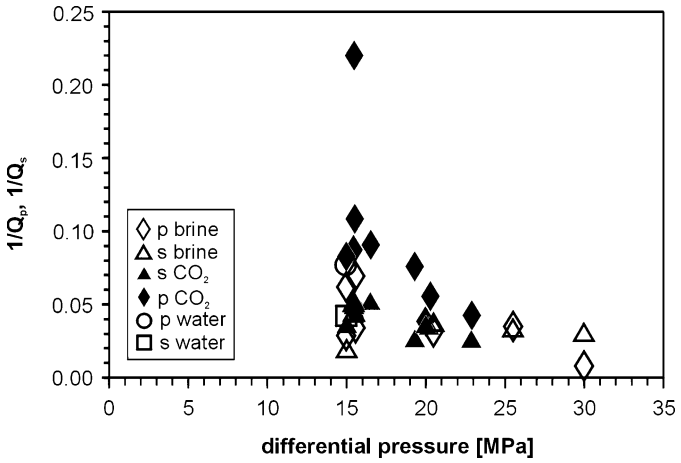

Figure 10: Seismic wave attenuation of sample BW3 as function of the differential pressure for various saturation conditions.

that is populated by $CO_{2,scr}$-saturated samples. This could be an indication of residual $CO_{2,scr}$ saturation or of alteration of the rock frame.

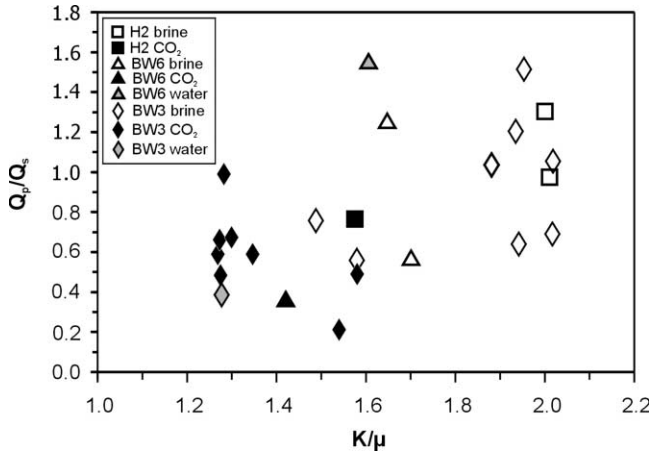

Figure 11: Classification of the saturation state using two seismic attributes. The upper right corner of the diagram is populated by data measured at brine saturation, while the lower left corner is mainly populated by data measured at $CO_{2,src}$ saturation.

Mineral Chemistry

During the experiment, fluid (brine) samples were taken from the collecting reservoir. Changes in the chemical composition of brine resulting from interaction with the sandstones H2, BW3 and BW6 are summarized in Figure 12A–C. The concentrations (mg/L) are normalized to the concentrations of initial 1 M NaCl brine. In contrast to the samples BW3 and BW6, aluminum and silicon were not analyzed in sample H2. The composition of the fluids before and after the reaction with sandstones is summarized in Tables 5–7. At similar duration, the contents of the analyzed cations in the fluids of the sandstone experiments are, with the

exception of Fe and Ni, higher than the contents of the dummy experiment. This behavior suggests that particularly the alteration and dissolution of the rock-bearing mineral phases are responsible for increasing cation contents. Steel corrosion is in most cases irrelevant for geochemical data interpretation.

TABLE 5
CHEMICAL COMPOSITION OF FLUID SAMPLES AFTER FOUR STAGES OF SATURATION OF THE SANDSTONE H2

Sample	**H2**		
	Saturation with 1 M NaCl	**Saturation with supercritical CO_2**	**Saturation with 1 M NaCl**
Ca	31	134	38
K	10	15	16
Mg	4.9	54	8.8
Mn	0.13	103	12
Zn	0.2	40	19
Li	0.1	0.2	0.1
Co	b.d.l.[a]	0.3	0.1
Ni	0.01	14	4.1
Cu	0.2	36	11
Mo	b.d.l.[a]	0.2	0.1
Cd	b.d.l.[a]	0.16	0.03
Pb	b.d.l.[a]	0.5	0.3

The cations were analyzed by ICP-MS and ICP-OES. The concentrations (mg/L) are normalized to the concentrations of initial 1 M NaCl brine.
[a] b.d.l., below detection limit.

TABLE 6
CHEMICAL COMPOSITION OF FLUID SAMPLES AFTER FOUR STAGES OF SATURATION OF THE SANDSTONE BW3

Sample	**L0 Initial brine**	**BW3**			
		Saturation with 1 M NaCl	**Saturation with supercritical CO_2**	**Saturation with 1 M NaCl**	**Saturation with supercritical CO_2**
Na	22,989[c]	n.a.[b]	n.a.[b]	n.a.[b]	n.a.[b]
Cl	35,453[c]	n.a.[b]	n.a.[b]	n.a.[b]	n.a.[b]
Ca	b.d.l.[a]	64	93	305	43
Fe	b.d.l.[a]	4.0	6.8	21	11
K	b.d.l.[a]	6.1	7.4	12	10
Mg	b.d.l.[a]	7.7	21	42	11
Mn	b.d.l.[a]	3.9	4.7	1.4	25
Si	b.d.l.[a]	6.1	10	24	14
Al	0.05	0.06	0.2	0.2	2.4
Zn	0.1	1.9	0.43	0.91	2.5
Co	b.d.l.[a]	b.d.l.[a]	0.41	0.38	2.7
Ni	b.d.l.[a]	0.8	5.0	2.3	14.6
Cu	b.d.l.[a]	0.1	3.0	2.5	4.4
Rb	<0.1	<0.1	0.1	<0.1	0.1
Sr	<0.1	1.2	1.4	0.9	0.7

(*continued*)

TABLE 6
CONTINUED

Sample	L0 Initial brine	BW3			
		Saturation with 1 M NaCl	Saturation with supercritical CO_2	Saturation with 1 M NaCl	Saturation with supercritical CO_2
Mo	b.d.l.[a]	0.1	0.2	<0.1	0.3
Cd	<0.01	0.02	0.10	0.02	0.04
Pb	b.d.l.[a]	b.d.l.[a]	0.41	0.50	1.75
Sn	b.d.l.[a]	b.d.l.[a]	b.d.l.[a]	b.d.l.[a]	b.d.l.[a]
Cs	b.d.l.[a]	b.d.l.[a]	b.d.l.[a]	b.d.l.[a]	b.d.l.[a]
Tl	b.d.l.[a]	b.d.l.[a]	b.d.l.[a]	b.d.l.[a]	b.d.l.[a]
Th	b.d.l.[a]	b.d.l.[a]	b.d.l.[a]	b.d.l.[a]	b.d.l.[a]
U	b.d.l.[a]	b.d.l.[a]	b.d.l.[a]	b.d.l.[a]	b.d.l.[a]

The cations were analyzed by ICP-MS and ICP-OES. The concentrations (mg/L) are normalized to the concentrations of initial 1 M NaCl brine.
[a] b.d.l., below detection limit.
[b] n.a., not analyzed.
[c] Na and Cl contents of the initial brine are calculated.

TABLE 7
CHEMICAL COMPOSITION OF FLUID SAMPLES AFTER FOUR STAGES OF SATURATION OF THE SANDSTONE BW6

Sample	BW6		
	Saturation with 1 M NaCl	Saturation with supercritical CO_2	Saturation with 1 M NaCl
Ca	65	77	123
Fe	45	b.d.l.[a]	2.1
K	7.6	6.1	8.9
Mg	8.7	7.7	9.3
Mn	4.6	0.45	0.19
Si	21	4.0	8.4
Al	0.3	0.1	0.1
Zn	3.9	1.8	0.4
Co	0.65	0.16	b.d.l.[a]
Ni	51	11.4	0.3
Cu	5.8	3.8	0.7
Rb	0.2	0.2	0.2
Sr	0.5	0.6	0.4
Mo	1.5	0.2	<0.1
Cd	0.02	0.03	0.01
Pb	0.12	0.02	0.01
Sn	b.d.l.[a]	b.d.l.[a]	b.d.l.[a]
Cs	b.d.l.[a]	b.d.l.[a]	b.d.l.[a]
Tl	b.d.l.[a]	b.d.l.[a]	b.d.l.[a]
Th	b.d.l.[a]	b.d.l.[a]	b.d.l.[a]
U	b.d.l.[a]	0.02	b.d.l.[a]

The cations were analyzed by ICP-MS and ICP-OES. The concentrations (mg/L) are normalized to the concentrations of initial 1 M NaCl brine.
[a] b.d.l., below detection limit.

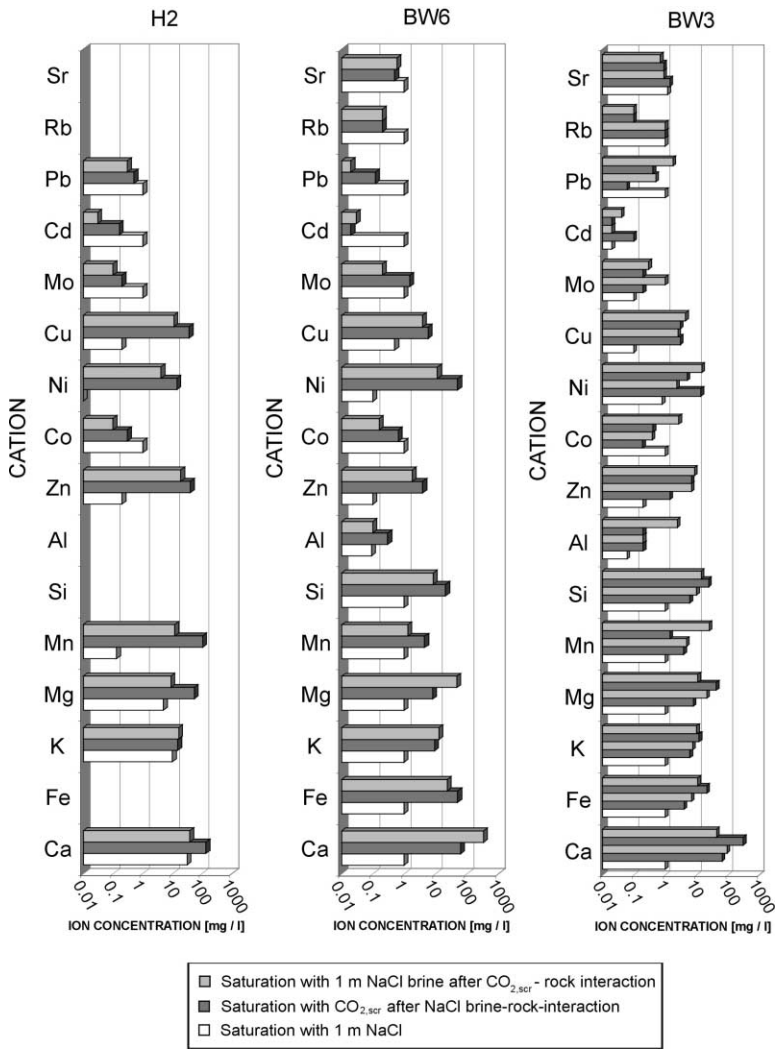

Figure 12: Bar graphs of the samples H2, BW6 and BW3, which indicate changes in the element composition of brine resulting from interaction with the sandstones. Fe, Si, Al, Rb and Sr contents were not analyzed for sample H2.

Figure 12A–C display the stages (steps) of saturation. As a result of the reaction with the brine, Ca, Fe, K, Mg, Mn, Si, Al, Zn, Co, Ni, Cu, Rb, Sr, Mo, Cd and Pb were leached in measurable amounts (see Tables 5–7 and Figure 12A–C). While all sandstone samples also contain Sn, Cs, Tl, Th and U (Table 8 and authors' unpublished data), there is no significant indication for mobilization of these cations during the reaction with 1 M NaCl brine and/or $CO_{2,scr}$. The leaching behavior of the cations is uneven and depends mainly on the following attributes:

- mineral composition of the rock,
- duration of fluid contact,
- pH,
- concentration and composition of the brine.

The highest leaching rate was observed during the rock–$CO_{2,scr}$ interaction in nearly all cases (Figure 12A–C and Tables 5–7). As observed during the dummy experiment and described in Ref. [21], there was a noticeable drop in pH after the injection of $CO_{2,scr}$ as a result of an increase in total HCO_3^- concentration. Such a decrease in pH resulted in primary mineral dissolution, e.g. carbonates.

TABLE 8
MAJOR AND TRACE ELEMENT DATA FOR RESERVOIR ROCK SAMPLE H2

Sample	**H2**		
	Composition before reaction with brine and supercritical CO_2	**Composition after reaction with brine and supercritical CO_2**	**Percentage increase (+) and decrease (−) in composition of sample H2 after reaction with 1 M NaCl brine and supercritical CO_2**
SiO_2 (wt%)	88.2	89.8	+1.8
TiO_2 (wt%)	0.88	0.22	−75.3
Al_2O_3 (wt%)	5.26	5.07	−3.6
Fe_2O_{3tot}(wt%)	0.87	0.59	−31.7
MnO (wt%)	0.013	0.002	−82.1
MgO (wt%)	0.31	0.25	−18.8
CaO (wt%)	0.25	0.14	−45.0
Na_2O (wt%)	0.09	0.11	+23.2
K_2O (wt%)	2.44	2.49	+2.2
P_2O_5 (wt%)	0.14	0.08	−45.2
H_2O^+ (wt%)	1.11	1.02	−8.6
CO_2 (wt%)	0.41	0.34	−16.7
Total	99.96	100.09	–
Cr (ppm)	19	19	+1.3
Ni (ppm)	11	21	+99.4
V (ppm)	14	10	−27.8
Co (ppm)	2.1	1.3	−38.1
Cu (ppm)	57	37	−35.1
Zn (ppm)	70	54	−23.4
Sr (ppm)	56	50	−10.7
Cs (ppm)	3.3	3.1	−6.1
Ba (ppm)	393	400	+1.8
Pb (ppm)	23	15	−34.8
Th (ppm)	13	4.2	−67.7
U (ppm)	4.4	1.3	−70.5
Li (ppm)	18	16	−11.1
Sn (ppm)	3.0	2.0	−33.3
Mo (ppm)	1.0	0.3	−70.0
Cd (ppm)	0.07	b.d.l.[a]	–
Sb (ppm)	0.8	0.5	−37.5
Tl (ppm)	0.6	0.6	+/−0.0
Bi (ppm)	0.03	0.01	−66.7

The major elements were analyzed by X-ray fluorescence (XRF) and all trace elements were analyzed by inductively coupled plasma mass spectrometry (ICP-MS). H_2O and CO_2 contents were measured with infrared spectrometry.

[a] b.d.l., below detection limit.

XRD analyses indicate that the duration of the experiments was too short to form measurable amounts of secondary mineral phases. For this reason the whole rock composition of sample H2 was analyzed by XRF and ICP-MS before and after the experiment to get an indirect indication on the changes in mineral composition. The whole rock data of sample H2 together with the relative changes in composition are summarized in Table 8.

In comparison with the initial composition of sample H2, most of the major elements and trace elements have lower concentrations (Table 8). However, SiO_2, Na_2O and K_2O content increases during the reaction with brine and $CO_{2,scr}$. Furthermore, the carbonate contents of reservoir rock H2 decreased after the reaction with brine and supercritical CO_2. As a result, dissolution prevails over precipitation of rock-bearing carbonates in this initial pre-steady-state experimental investigation. Decreasing H_2O^+ (structural water) contents suggest reaction of OH-bearing minerals (e.g. sheet silicates) with $CO_{2,scr}$.

CONCLUSIONS

The geochemical data show that the exposure of sandstone to brine and $CO_{2,scr}$ under temperature and pressure conditions that are representative for depths below 1000 m leads to the mobilization of a number of different ions from the rock's mineral framework. This may be seen as an indication for mineral dissolution. Mineral precipitation has not been found for the duration of our experiments (up to 10 days). These findings suggest an increase of the porosity and consequently of the hydraulic permeability. These effects are probably too small to be detected using seismic methods, at least during short-term experiments.

The seismic data show a dependence of both the bulk and the shear moduli on the saturation state as well as on the (differential) pressure. The Gassmann model underestimates the fluid substitution effect by an amount that is representative for the modulus dispersion between the static regime (Gassmann model) and the ultrasonic frequency range (laboratory data). The dependence of the shear modulus on the saturating fluid is not predicted by the Gassmann model. The shear modulus shows a higher pressure sensitivity than the bulk modulus. This may lead to the discrimination of pressure and saturation effects through the simultaneous use of compressional and shear waves. The seismic wave attenuation shows the potential to contribute useful information about the saturation state. The experiments corroborate numerical studies that predict fluid front instabilities—and thus breakthrough saturation below 1—when $CO_{2,scr}$ displaces brine. The application of geophysical methods for in situ reservoir monitoring requires the calibration of all effects in laboratory experiments for each reservoir rock, taking into account the different length scales and frequency ranges. The assessment of the reservoir state will certainly benefit from the incorporation of further geophysical methods, such as electrical resistivity and gravity methods.

RECOMMENDATIONS

We recommend effort and funding be directed toward the following laboratory research:

- long-term experiments (several months),
- investigation of fluid-phase behavior (e.g. solubility of $CO_{2,scr}$ in brine),
- pH and electrical resistivity measurements,
- porosity and permeability evolution in triaxial cell, mercury porosimetry,
- assessment of fluid displacement process (fluid front instabilities, fingering),
- cap rock experiments.

ACKNOWLEDGEMENTS

The contributions of the GFZ Potsdam to the Carbondioxide Capture Project (CCP) were initiated and directed by Prof. Dr G. Borm, Prof. Dr J. Erzinger and Dr E. Huenges.

The authors wish to thank Rudolf Naumann for performing the XRF analyses. We are grateful to Knut Hahne, Heike Rothe (ICP-MS) and Sabine Tonn (ICP-OES) for their help with analyses at the GeoForschungsZentrum Potsdam. The sandstone samples along with poro-perm data were provided by Ute Trautwein. Liane Liebeskind and Olaf Ryll helped with the experiments in the triaxial cell. Many thanks to

Siegfried Raab for his patience in endless discussions concerning the improvement of the experimental setup.

We are very grateful for the comments and suggestions by Curt Oldenburg and two anonymous reviewers.

REFERENCES

1. A. Seibt, T. Kellner, P. Hoth, in: P. Hoth, A. Seibt, T. Kellner, E. Huenges (Eds.), *Geothermie Report 97-1: Geowissenschaftliche Bewertungsgrundlagen zur Nutzung hydrogeothermaler Ressourcen in Norddeutschland*, Scientific Technical Report STR97/15, 1997, pp. 134–146.
2. D. Naumann, Salinare tiefenwässer in Norddeutschand, Scientific Technical Report STR00/21, 2000, p. 116.
3. T. Clifford, Fundamentals of Supercritical Fluids, Oxford University Press, New York, 1998.
4. R.L. Folk, *Am. J. Sci.* **245** (1947) 388–394.
5. W.D. Grimm, Bildatlas Wichtiger Denkmalgesteine der Bundesrepublik Deutschland, Bayerisches Landesamt für Denkmalpflege, Arbeitsheft 50, 1990.
6. F.J. Pettijohn, P.E. Potter, R. Siever, Sand and Sandstone, Springer, New York, 1987.
7. M. Alber, J. Heiland, *Rock Mech. Rock Eng.* **34** (2001) 167–186.
8. G. Mavko, T. Mukerji, J. Dvorkin, The Rock Physics Handbook, Cambridge University Press, New York, 1998.
9. H.G. Plessen, H. Rothe, M. Zimmer, J. Erzinger, in: K. Govindaraju, P.J. Potts, P.C. Webb, J.S. Watson (Eds.), *Geostandard Newsletters*, 18, 1994, pp. 211–300.
10. M. Ferer, G.S. Bromhal, D.H. Smith, *J. Energy Environ. Res.* **2** (2001) 120–132.
11. R.J. Glass, M.J. Nicholl, *Geoderma* **70** (1996) 133–163.
12. R. Lenormand, E. Touboul, C. Zarcone, *J. Fluid Mech.* **180** (1988) 165–187.
13. Y. Guéguen, V. Palciauskas, Introduction to the Physics of Rocks, Princeton University Press, Princeton, NJ, 1994.
14. Z. Wang, M.E. Cates, R.T. Lagan, *Geophysics* **63** (1998) 1604–1617.
15. K. Aki, P.G. Richards, Quantitative Seismology: Theory and Methods, W.H. Freeman and Co., New York, 1980.
16. M.A. Biot, *J. Acoust. Soc. Am.* **28** (1956) 168–191.
17. R.D. Stoll, Sediment Acoustics, Springer, Berlin, 1989.
18. A.-M. Wulff, H. Burkhardt, *J. Geophys. Res.* **102** (1997) 3043–3050.
19. W.F. Murphy, K.W. Winkler, R.L. Kleinberg, *Geophysics* **51** (1986) 757–766.
20. J. Dvorkin, R. Nolen-Hoeksema, A. Nur, *Geophysics* **59** (1994) 428–438.
21. J.P. Kaszuba, D.R. Janecky, M.G. Snow, *Appl. Geochem.* **18** (2003) 1065–1080.